Hybrid Density Functional Study of the *p*-Benzosemiquinone Anion Radical: The Influence of Hydrogen Bonding on Geometry and Hyperfine Couplings

Patrick J. O'Malley

Department of Chemistry, University of Manchester Institute of Science and Technology, Manchester, M60 1QD, England

Received: April 10, 1997; In Final Form: June 25, 1997[⊗]

Hybrid density functional calculations (B3LYP) are performed on the *p*-benzosemiquinone anion radical in its free and hydrogen-bonded forms. Geometries and hyperfine couplings are reported. A variety of basis sets ranging from split valence to full triple-ζ are employed. Converged results for hyperfine couplings are observed at the double-ζ level. Hydrogen bonding principally leads to increased spin density on the carbonyl carbon leading to an increase in the ^{13}C isotropic and anisotropic hyperfine coupling of this atom. Comparison with experimentally determined isotropic and anisotropic hyperfine couplings shows good quantitative agreement between theoretical calculation and experiment.

Introduction

Quinones are ubiquitous to living systems and represent important cofactors for electron transfer in photosynthesis and respiration.[1] In photosynthesis, for example, quinones act as electron acceptors in the initial charge separation. For both bacterial and higher plant Photosystem 2 two quinones termed Q_a and Q_b act in concert to enable efficient charge separation to take place.[2] Q_a is initially reduced to form the semiquinone anion radical. This then forwards its electron to Q_b forming the Q_b semiquinone anion radical. On further charge separation Q_a accepts another electron to form the semiquinone anion radical again. This electron is then passed on to the already reduced Q_b to give the Q_b^{2-} dianion. This then accepts two protons to form QH_2 which leaves the protein site to be replaced by another quinone molecule from a quinone pool nearby.

Q_a and Q_b are often identical quinones; plastoquinone in higher plants and ubiquinone in bacterial systems. Their differing functions and properties are therefore conferred by their interactions with their protein environment. A variety of spectroscopic methods, most notably EPR, ENDOR, FTIR, and NMR, have been used to investigate such differences.[3−5] Differences in the hydrogen bonding ability of both quinones is generally put forward for the differing functions observed, i.e., specific hydrogen bonds to nearby amino acid residues are able to tailor the quinone to perform a specific function.

In this study we use modern density functional methods to examine the structure, and hyperfine couplings of the parent semiquinone anion, *p*-benzosemiquinone (Figure 1). First principles electronic structure methods provide a unique probe into the electronic influence of hydrogen bonding on the electronic structure of quinones and their semiquinone anion forms. It is imperative to perform an in-depth study of the parent unsubstituted form initially to investigate the key electronic structure factors which change on hydrogen-bond formation. This study will also permit us to test the most appropriate electronic structure method for later study of larger quinones. Such information will thereby form the basis for the interpretation of future studies on the more highly substituted, less symmetrical forms. The influence of hydrogen bonding on the calculated hyperfine couplings is primarily studied.

Hybrid density functional methods, particularly the B3LYP functional, are increasingly being shown to provide excellent

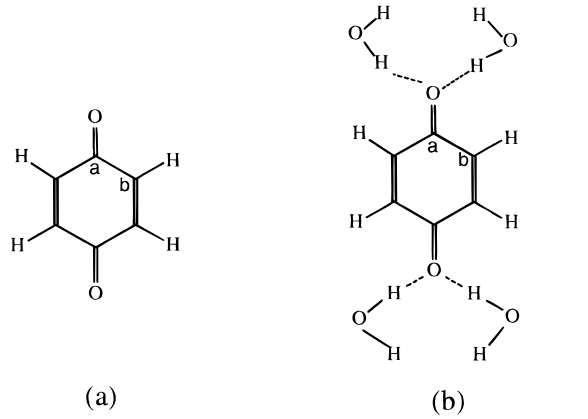

Figure 1. *p*-Benzosemiquinone (a) and its hydrogen-bonded complex with four water molecules (b). D_{2h} point group symmetry.

electronic structures for nonradicals and radicals alike.[6,7,8] They are uniquely capable of giving highly accurate descriptions of free radical properties such as isotropic and anisotropic hyperfine coupling constants.[8,9] Nuclear hyperfine couplings consist of an isotropic (Fermi contact) and anisotropic(dipolar) terms. In the electronic structure calculation both are calculated separately. Experimentally, in liquid solution, rapid tumbling leads to elimination of the anisotropic component and the isotropic value is measured in isolation. For solid-state studies both the isotropic and anisotropic terms contribute to the coupling, and the total tensor is the experimental observable.

For calculation purposes the 3×3 hyperfine interaction tensor can be separated into its isotropic (spherically symmetric) and anisotropic (dipolar) components. To first-order isotropic hyperfine interactions, $A_{iso}(N)$ are related to the spin densities, $\rho^s(r_N)$, at the corresponding nuclei by

$$A_{iso}(N) = (8\pi/3) g_e g_N \beta\beta_N \rho^s(r_N)$$

The anisotropic components are derived from the classical expression of interacting dipoles:

$$T_{ij}(N) = g_e g_N \beta\beta_N \sum P^{\alpha-\beta}{}_{\mu\nu} \langle \varphi_\mu | \, r^{-5}{}_{kN} (r^2{}_{kN} \delta_{ij} - 3 r_{kNi} r_{kNj}) | \varphi_\nu \rangle$$

The isotropic component can be obtained form the Fermi contact analysis given by most modern electronic structure

[⊗] Abstract published in *Advance ACS Abstracts,* August 1, 1997.

S1089-5639(97)01238-3 CCC: $14.00

TABLE 1: Optimized Bond Distances and Angles of Hydrogen-Bonded and Free p-Benzosemiquinone Anion Radicals of Figure 1 Using Different Basis Sets[a]

bond/angle	PM3	6-31G+G(d)	EPR-II	EPR-III
Ca−O	1.25 (1.26)	1.27 (1.28)	1.27 (1.29)	1.26 (1.28)
Ca−Cb	1.45 (1.45)	1.45 (1.44)	1.47 (1.45)	1.45 (1.44)
Cb−Cb	1.36 (1.36)	1.37 (1.37)	1.38 (1.38)	1.37 (1.37)
O−H(hb)	(1.78)	(1.79)	(1.78)	(1.79)
C*a*OH(hb)	(121.3)	(122.3)	(124.1)	(123.0)

[a] Functional used for all calculations, except PM3, is B3LYP. Distances in angstroms and angles in degrees. Hydrogen-bonded complex (Figure 1b) values are given in brackets.

TABLE 2: UB3LYP/EPR-II//UB3LYP/EPR-II Calculated Hyperfine Couplings (MHz)[a]

position	isotropic coupling A_{iso}	anisotropic coupling T_{11} T_{22} T_{33}	total coupling A_{11} A_{22} A_{33}
O	−20.1(−21.0)	41.7(37.0)	21.6(17.0)
		41.1(36.3)	21.0(16.3)
		−82.9(−75.4)	−103.0(−96.4)
H	−6.5(−6.2)	−3.4(−3.4)	−9.9(−9.6)
		−2.3(−2.5)	−8.8(−8.7)
		5.6(5.9)	−0.9(−0.3)
Ca	−10.3(−4.2)	−8.2(−12.1)	−18.5(−16.3)
		−4.2(−9.1)	−14.5(−13.3)
		12.3(21.1)	2.0(16.9)
Cb	−0.3(−1.5)	−7.0(−6.5)	−7.3(−8.0)
		−6.7(−6.1)	−7.0(−7.6)
		13.7(12.6)	13.4(11.1)
H(hb)	(0.2)	(6.3)	(6.5)
		(−3.1)	(−2.9)
		(−3.1)	(−2.9)

[a] The values for the hydrogen-bonded complex (Figure 1b) are given in brackets.

programs. The anisotropic components can be obtained from the spin-only electric field gradient tensors.

Methods

The *p*-benzosemiquinone radical is shown in Figure 1a together with the numbering scheme used. A hydrogen-bonded complex with four water molecules (Figure 1b) was used to model hydrogen bonding interactions.

All studies utilized the B3LYP hybrid functional[10] as implemented on GAUSSIAN 94(11). The calculations used the 6-31+G(d),[11] EPR-II[9] and EPR-III[9] basis sets. The EPR basis sets are particularly appropriate for calculation of Fermi contact terms. Comparative studies were also performed using the semiempirical PM3 method. Long-range environmental effects on hyperfine couplings were estimated using the self-consistent isodensity polarizable continuum model (SCIPCM).[12]

All calculations were performed using GAUSSIAN 94(11). Graphical representations of orbitals and spin densities were generated using SPARTAN.[13] The calculations were run on DEC and Silicon Graphics workstations.

Results and Discussion

Geometry. Selected bond distances and angles for *p*-benzosemiquinone, both hydrogen-bonded and non-hydrogen-bonded, are given in Table 1. No major changes are brought about on the internal geometry of the *p*-benzosemiquinone molecule as a result of hydrogen bond formation. The only significant change is a slight lengthening of the C*a*−O bond.

From Table 1 it is of note that the PM3 method compares favorably with the higher level methods. Of particular note is the ability of the method to provide accurate representation of the hydrogen-bonding interaction. Clearly this is of some significance for future calculations on larger less symmetrical quinones where the density functional calculation of optimized geometries may be infeasible because of computer cost.

Spin Densities and Hyperfine Couplings. The isotropic, anisotropic, and total(isotropic plus anisotropic) hyperfine couplings calculated for the *p*-benzosemiquinone anion radical are given in Tables 2 −6. A variety of methods were used to calculate the hyperfine couplings to understand the effect of basis set and geometry on such couplings. In line with accepted notation the method after the double slash signifies the geometry optimization level with the method before the slashes signifying the level of theory used to calculate the hyperfine couplings:

1. UB3LYP/EPR-II//UB3LYP/EPR-II

2. UB3LYP/EPR-III//UB3LYP/EPR-III

3. UB3LYP/6-31G+G(d)//UB3LYP/6-31G+G(d)

4. UB3LYP/EPR-III//PM3

5. UB3LYP(SCIPCM)/EPR-II//UB3LYP/EPR-II

The second method uses a very large triple-ζ basis set and would be expected to provide the most accurate geometries and couplings. It has already been shown to perform admirably in the calculation of atomic and small-molecule hyperfine couplings.[9] The smaller double-ζ basis set EPR−II is more economical and has already been shown to produce results of similar quality to EPR−III for smaller radicals.[9] The 6-31G+G(d) basis set is again more economical than the EPR−II basis set and is of interest from a test of more general basis sets in the calculation of hyperfine couplings. Method 4 is used mainly in anticipation of difficulties in calculating geometries for the unsymmetrical highly substituted quinones at the density functional level. Here the PM3 method is used for geometry optimization followed by single-point density functional calculations. An alternative here would be use of smaller basis set density functional calculations for the geometry optimizations. Intermolecular interactions are modeled poorly by such small basis sets, and considerable stabilization of hydrogen-bonded complex is found due to basis set superposition. This in general leads to overly short intermolecular hydrogen bonds.[8] The parametrization of the PM3 method overcomes such difficulties.[14] Comparison between results for the EPR−II and EPR−III basis sets shows that very similar results are obtained. Indeed it can be said that converged results are observed at the EPR−II level for all couplings. For the 6-31+G(d) basis set, Table 4 shows that good agreement for the proton couplings is observed when compared with EPR−III. For ^{17}O and ^{13}C the agreement with the larger basis sets is poor in particular for the ^{13}C couplings.

Of particular note are the hyperfine couplings obtained using the UB3LYP/EPR−II//UPM3 method, (Table 5). The hyperfine couplings are in excellent agreement with the values calculated by UB3LYP/EPR-II//UB3LYP/EPR-II. Clearly this may be the method to adopt for hyperfine coupling calculation on larger more unsymmetrical semiquinone anions present in biological samples.

Because of the similarity of the hyperfine couplings calculated by all methods this discussion will be confined to an analysis of the UB3LYP/EPR−II//UB3LYP/EPR−II data (Table 2). This method gives quality results similar to the more expensive UB3YP/EPR-III//UB3LYP/EPR-III set and represents an ideal

TABLE 3: UB3LYP/EPR-III//UB3LYP/EPR-III Calculated Hyperfine Couplings(MHz)[a]

position	isotropic coupling A_{iso}	anisotropic coupling T_{11} T_{22} T_{33}	total coupling A_{11} A_{22} A_{33}
O	−22.1(−22.0)	43.6(39.8)	21.5(17.8)
		42.7(39.0)	20.6(17.0)
		−86.3(−78.7)	−108.4(−100.7)
H	−6.7(−6.4)	−3.4(−3.5)	−10.1(−9.9)
		−2.2(−2.4)	−8.9(−8.8)
		5.7(5.9)	−1.0(−0.5)
Ca	−9.1(−3.8)	−9.1(−13.0)	−18.2(−16.8)
		−4.9(−9.7)	−14.0(−13.5)
		14.1(22.8)	5.0(19.0)
Cb	−0.6(−1.6)	−7.4(−6.9)	−8.0(−8.5)
		−7.1(−6.5)	−7.7(−8.1)
		14.4(13.3)	13.8(11.7)
H(hb)	(0.1)	(6.1)	(6.2)
		(−3.0)	(−2.9)
		(−3.0)	(−2.9)

[a] The values for the hydrogen-bonded complex (Figure 1b) are given in brackets.

TABLE 4: UB3LYP/6-31G+G(d)//UB3LYP/6-31G+G(d) Calculated Hyperfine Couplings (MHz)[a]

position	isotropic coupling A_{iso}	anisotropic coupling T_{11} T_{22} T_{33}	total coupling A_{11} A_{22} A_{33}
O	−28.0(−27.0)	39.3(35.6)	11.3(8.6)
		38.3(34.8)	10.3(7.8)
		−77.7(−70.3)	−105.7(−97.3)
H	−6.9(−6.5)	−3.1(−3.2)	−10.0(−9.7)
		−2.5(−2.7)	−9.4(−9.2)
		5.7(5.8)	−1.2(−0.7)
Ca	−0.7(6.3)	−8.4(−12.1)	−9.1(−5.8)
		−3.4(−8.9)	−5.1(−2.6)
		12.8(20.9)	12.1(27.2)
Cb	4.1(2.8)	−6.6(−6.1)	−2.5(−3.3)
		−6.2(−5.7)	−2.1(−2.9)
		12.8(11.7)	16.9(14.5)
H(hb)	(0.1)	(6.1)	(6.2)
		(−3.1)	(−3.0)
		(−3.1)	(−3.0)

[a] The values for the hydrogen-bonded complex (Figure 1b) are given in brackets.

efficient method for the theoretical calculation of hyperfine couplings for medium-sized radicals.

To interpret the calculated hyperfine couplings, we make use of the orbitals and spin density plots of Figures 2−4. The highest occupied molecular orbital for the *p*-benzosemiquinone radical is shown in Figure 2

. The orbital is bonding between C*a* and C*b* and nonbonding between the two C*b* atoms and C*a* and O. In Figures3 and 4 the unpaired spin density plots(alpha−beta) are contoured at two levels, 0.002 and 0.01 e/au^3. The 0.01 e/au^3 plot (Figure 4) powerfully demonstrates the effect of hydrogen bonding on the distribution of unpaired spin. For the non-hydrogen-bonded, "free" case the unpaired spin is concentrated at the O atom positions. Much lower concentrations are found at the C*a* and C*b* locations. Closer examination of the plots does indicate slightly higher spin at C*b*. On hydrogen-bond formation (Figure 4), clearly shows an enhanced spin density at the C*a* position. A decrease in the C*b* and O positions accompanies this. The major effect of hydrogen bonding is therefore an increased spin density at the C*a* positions at the expense of a decrease in the O (primarily) and C*b* locations.

TABLE 5: UB3LYP/EPR-II// UPM3 Calculated Hyperfine Couplings(MHz)[a]

position	isotropic coupling A_{iso}	anisotropic coupling T_{11} T_{22} T_{33}	total coupling A_{11} A_{22} A_{33}
O	−20.1(−19.9)	41.4(38.0)	21.3(18.1)
		40.8(37.3)	20.7(17.4)
		−82.1(−75.4)	−102.2(−95.3)
H	−6.7(−6.4)	−3.4(−3.5)	−10.1(−9.9)
		−2.3(−2.5)	−9.0(−8.9)
		5.7(5.9)	−1.0(−0.5)
Ca	−10.1(−5.2)	−8.3(−11.7)	−18.4(−16.9)
		−4.3(−8.5)	−14.4(−13.7)
		12.5(20.1)	2.5(14.9)
Cb	−0.4(−1.4)	−7.0(−6.7)	−7.4(−8.1)
		−6.8(−6.3)	−7.2(−7.7)
		13.8(13.0)	13.4(11.6)
H(hb)	(0.1)	(6.5)	(6.6)
		(−3.0)	(−2.9)
		(−3.0)	(−2.9)

[a] The values for the hydrogen-bonded complex (Figure 1b) are given in brackets.

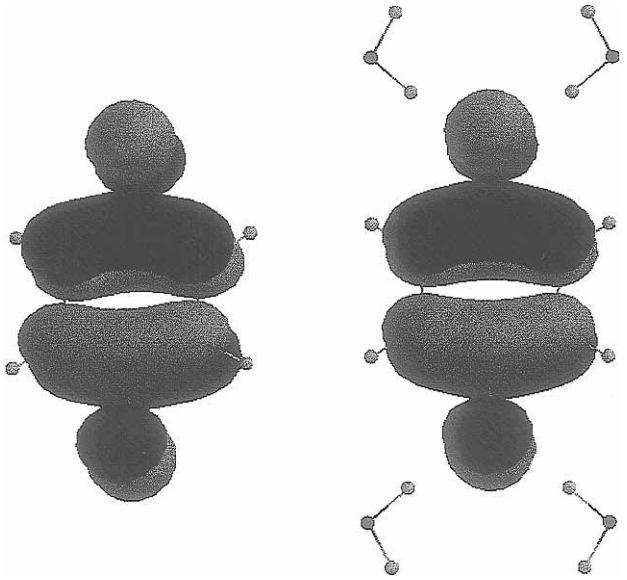

Figure 2. α highest occupied molecular orbital for *p*-benzosemiquinone at UB3LYP/EPR-II//UB3LYP/EPR-II level contoured at 0.002 e/au^3. The radical orientation is as shown in Figure 1.

These spin density plots an now be used to interpret the calculated isotropic and anisotropic hyperfine couplings of Table 2. From Table 2 we can see that hydrogen bonding affects all coupling to some extent. The isotropic and anisotropic hyperfine couplings for the ring hydrogen atom remain essentially unchanged on hydrogen-bond formation. Hydrogen bonding leads to a slight decrease in the anisotropic components of the O coupling. The C*b* and particularly the C*a* couplings are particularly sensitive to hydrogen bonding. For C*b* the principal change occurs for the isotropic coupling which decreases −0.3 to −1.5 MHz on hydrogen-bond formation. The anisotropic couplings are relatively unchanged however. For C*a* dramatic changes in both isotropic and anisotropic hyperfine couplings occur.

The isotropic (Fermi contact) arises from the presence of finite unpaired electron spin density at the nucleus in question. The unpaired electron is situated in a π-type orbital (Figure 2) and hence unpaired electron spin density arises at the nuclear positions via spin polarization mechanisms.[15] The anisotropic couplings are, on the other hand, a direct measure of the

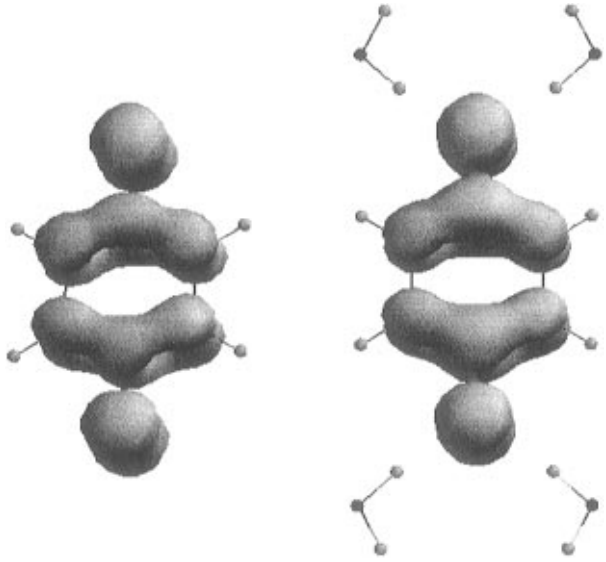

Figure 3. The 0.002 electrons/au^3 unpaired spin density contour. UB3LYP/EPR-II//UB3LYP/EPR-II. Hydrogen-bonded complex (Figure 1b) on right-hand side.

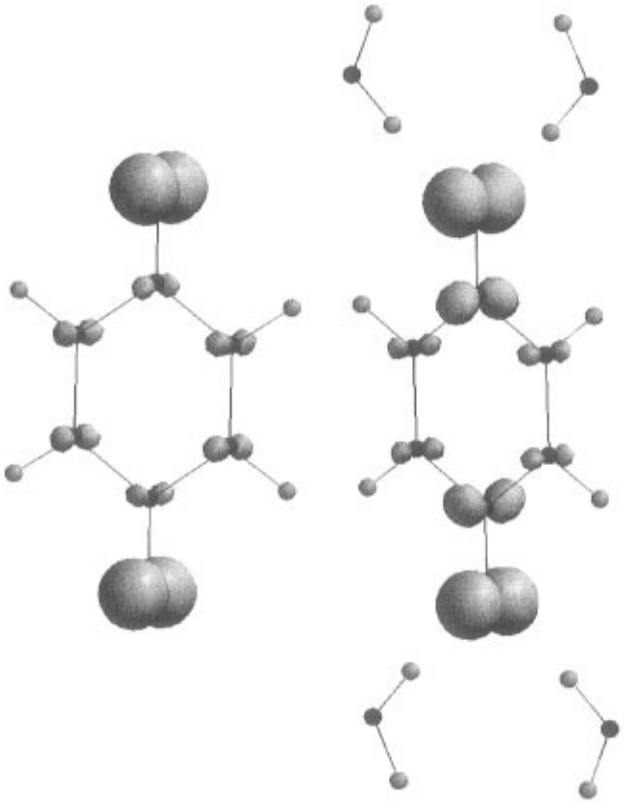

Figure 4. 0.01 electrons/au^3 unpaired spin density contour. UB3LYP/EPR-II//UB3LYP/EPR-II. Hydrogen-bonded complex (Figure 1b) on right-hand side.

interaction of the unpaired electron in the π orbital with the nuclei. Prevously in the absence of accurate molecular wave functions these anisotropic hyperfine interactions have been explained by assuming that the p type molecular orbital near the nuclear positions can be approximated by atomic p type functions.[15] For the oxygen atoms such a situation does indeed exist due to the nonbonding nature of the out-of-plane p orbital on the oxygen atom (Figure 2). The anisotropic coupling of the oxygen atoms will be dominated by the large concentration of unpaired spin density. As expected from the shape of the unpaired spin density plots (Figures 3 and 4), an axial tensor is obtained for this coupling. Hydrogen-bond formation leads to a slight decrease in the anisotropic coupling of the oxygen atom (Table 2). This can be directly correlated with a decrease in spin density at the oxygen atom on hydrogen bond formation referred to above.

For the C*a* and C*b* atoms the situation is somewhat different. Here a relatively low unpaired spin density, compared with the O atom, exists at both of these atoms in the non-hydrogen-bonded state (Figure 4). Because of the imbalance in spin density between the O and C*a* atom positions, the high concentration of spin density near the O atom can be expected to contribute significantly to the anisotropic coupling of C*a*. In addition there exists some spin density along the C*a*−C*b* bond (Figure 3) which may also contribute to the ^{13}C anisotropic coupling of the Ca atom. These factors are reflected in the rhombic symmetry of the C*a* anisotropic coupling tensor as opposed to the axial tensor that would be expected from it own unpaired spin density. Hydrogen-bond formation leads to a substantial change in the C*a* anisotropic ^{13}C tensor principal values, (Table 2). The values are significantly increased, and the tensor assumes more axial nature. This is explained by the spin density plots of Figure 4; increased spin density at C*a* on hydrogen bonding leads directly to increased anisotropic couplings plus the greater contribution from the atoms own spin density will lead to a more axial tensor.

For the C*b* position an essentially axial anisotropic tensor for both hydrogen bonded and non-hydrogen-bonded cases Table 2). Here the distance from the O atom precludes any major contributions from this spin density to C*b*'s anisotropic coupling. The small decrease in coupling observed on hydrogen-bond formation is a reflection of the slight decrease in spin density value demonstrated in Figure 4.

On the basis of the above analysis of the anisotropic couplings, it is now possible to discuss the trends in the isotropic couplings. Such couplings are caused by spin density appearing directly at the nucleus in question, which arises in this case via spin polarization mechanisms.[15]

The ^{13}C isotropic coupling for C*a* and C*b* are both negative negative in the non-hydrogen-bonded case (Table 2). This is a reflection of excess negative spin density at these nuclei. Spin polarization by the unpaired electron density of the atom's own π spin would be expected to contribute to excess of α spin giving rise to a positive isotropic coupling.[15] Spin polarization by the neighboring π spin density would be expected to give rise to excess β spin at the nuclear position leading to a negative hyperfine coupling. From the negative coupling observed (Table 2) therefore it would appear that the polarization by the neighboring atoms predominate giving rise to a negative isotropic hyperfine coupling for both C*a* and C*b* in the non-hydrogen-bonded state. For the oxygen atom the isotropic coupling arises primarily from spin polarization by the π-orbital lobe at the oxygen atom giving rise to an excess of α spin and hence for ^{17}O, a negative coupling constant.

On hydrogen-bond formation the ^{13}C isotropic coupling for C*a* becomes less negative while the C*b* isotropic coupling becomes more negative (Table 2). These can be directly related to the changes in anisotropic couplings referred to above. Increased π spin density at C*a* leads to an increased spin polarization by this spin density on the C*a* s orbitals. This will increase the positive contribution to the isotropic coupling. The change in coupling value from −10.3 to −4.2 is a consequence of this. For C*b* the isotropic coupling is more negative in the hydrogen-bonded state. This reflects the slight decrease in π spin density at C*b* leading to less positive contribution plus the increase in spin density at neighboring C*a* which increases the negative contribution. For the oxygen atom the isotropic

TABLE 6: UB3LYP(SCIPCM)/EPR-II//UB3LYP/EPR-II Calculated Hyperfine Couplings (MHz)[a]

position	isotropic coupling A_{iso}	anisotropic coupling T_{11} T_{22} T_{33}	total coupling A_{11} A_{22} A_{33}
O	−19.6(−20.8)	40.3(37.8)	20.7(17.0)
		39.8(37.1)	20.2(16.3)
		−80.1(−74.9)	−99.7(−95.7)
H	−6.2(−6.1)	−3.6(−3.4)	−9.8(−9.5)
		−2.5(−2.5)	−8.7(−8.6)
		5.4(5.8)	−0.8(−0.3)
Ca	−8.5(−3.9)	−9.3(−12.3)	−17.8(−16.2)
		−5.5(−9.3)	−14.0(−13.2)
		14.7(21.6)	6.2(17.7)
Cb	−0.7(−1.6)	−6.8(−6.4)	−7.5(−8.0)
		−6.5(−6.0)	−7.2(−7.6)
		13.3(12.5)	12.6(−10.9)
H(hb)	(0.2)	(6.3)	(6.5)
		(−3.1)	(−2.9)
		(−3.1)	(−2.9)

[a] The values in the brackets are for the complex of Figure 1b immersed in a continuous dielectric (ϵ) of 80.0 (water). For the non-hydrogen bonded state an ϵ value of 47.24 (DMSO see text and Table 7) was used using structure of Figure 1a.

TABLE 7: Comparison of Experimental and Calculated ^{1}H, ^{13}C, and ^{17}O Isotropic Hyperfine Couplings[a]

	experimental [b,c]		calculated	
atom	DMSO	DMSO/WATER	DMSO	WATER
O	−26.5	−24.4	−19.6	−20.8
Ca	−6.0	−1.8	−8.5	−3.9
Cb		−1.4	−0.7	−1.6
H	−6.8	−6.7	−6.2	−6.1

[a] All couplings are given in MHz. [b] Reference 18. [c] Reference 19.

coupling changes little after hydrogen-bond formation. Here the decrease in spin density at the oxygen atom is counterbalanced by the increased spin density at Ca, resulting in an essentially unchanged ^{17}O isotropic hyperfine coupling value.

Comparison with Experimental Data. Extensive liquid solution studies of the p-benzosemiquinone anion radical were carried out in the1960s.[16−19] ^{1}H, ^{13}C, and ^{17}O isotropic hyperfine couplings were determined in a wide range of solvents. In the 1980s powder ENDOR was used to obtain the ^{1}H isotropic and anisotropic hyperfine couplings in alcohol solvents.[20,21] From the proton data a direct comparison with the total tensors of Table 2 is possible. The experimental values reported for the hydrogen bonded proton in an alcohol matrix are 5.9, −2.9, and −2.9 MHz. These are in close agreement with the calculated values of Table 2. For the ring proton only two reliable principal hyperfine tensor values have been reported. These are −10.2 and −9.0 MHz, which are in excellent agreement with the calculated values of this study. The third tensor value is difficult to assign accurately due to the presence of a strong matrix ENDOR signal. It can confidently be predicted to be $<|1.0|$ MHz,[22] which is in accord with the calculated value of −0.3 MHz in Table 2. A situation such as this occurs frequently when analyzing powder ENDOR spectra. The ability to be able to quantitatively predict the principal values will be a significant help in the assignment of such spectra.

Isotropic hyperfine coupling data obtained for ^{17}O, ^{13}C and ^{1}H in water and dimethyl sulfoxide (DMSO) are summarized in Table 7 , where they are compared with the UB3LYP-(SCIPCM)/EPR−II//UB3LYP/PR−II calculated couplings of this study. Excellent agreement is observed for the ^{1}H couplings. Good agreement is observed for the ^{17}O coupling constant. For the C*b* position agreement between theory and experiment is again good. For the C*a* position comparison of the absolute values is reasonable between experimental and calculated. This coupling, as the above discussion emphasized, is extremely sensitive to hydrogen bonding. This has also been found to be the case experimentally; see Table 7. In addition in the liquid solution hydrogen bonding is likely to be a dynamical situation with rapid formation/breakup of the hydrogen bonded complexes occurring within the EPR time scale. This is to be contrasted to the static complex of Figure 1b used for calculation purposes. In addition for DMSO it cannot be ruled out that nonspecific molecular complexes are formed between the semiquinone and DMSO molecules. The calculation of the change in ^{13}C coupling in going from non-hydrogen-bonded to hydrogen-bonded, $\Delta^{13}C = +4.2$ MHz (experimentally, Table 7) and +4.6 MHz (theoretically, Table 7) indicates excellent agreement between theory and experiment.

Conclusions

Density functional calculations employing the B3LYP functional provide excellent hyperfine couplings and spin density distributions for the *p*-benzosemiquinone free radical. Detailed insights into the influence of hydrogen bonding on the electronic wave function are revealed. This study provides a firm grounding for the interpretation of hyperfine couplings and spin density distributions for the biologically important semiquinone radicals.

References and Notes

(1) *Functions of Quinones in Energy Conserving Systems*; Trumpower, B. L., Ed.; Academic Press: New York, 1986.

(2) Okamura, M. Y.; Feher G. *Annu Rev. Biochem.* **1992**, *61*, 861.

(3) van den Brink, J. S.; Spoyalov, A. P.; Gast, P.; van Liemt, W. B. S.; Raap, J.; Lugtenburg, J.; Hoff, A. J. *FEBS Lett.* **1994**, *353*, 272.

(4) Breton, J.; Burie, J.−R; Boullais, C.; Berger, G.; Nabedryck, E.; Mioskowski, C. *Biochemistry* **1994**, *33*, 14378.

(5) van Liemt, W. B. S.; Boender, G. J.; Gast, P.; Hoff, A. J.; Lugtenberg, J.; de Groot, H. M. J. *Biochemistry* **1995**, *34*, 10229.

(6) Adamo, C.; Barone, V.; Fortunelli, V. *J. Chem. Phys.* **1995**, *102*, 1689.

(7) O'Malley, P. J; Ellson, D. A. *Chem. Phys. Lett.* **1996**, *260*, 492.

(8) O'Malley, P. J. *Chem. Phys. Lett.* **1996**, *262*, 797.

(9) Barone, V. In *Recent Advances in Density Functional Methods*; Chong, D. P., Ed.; World Scientific Publishing: Singapore, 1995.

(10) Becke, A. D *J. Chem. Phys.* **1993**, *98*, 5648.

(11) Frisch, M. J.; Trucks G. W.; Schlegel, H. B.; Gill, P. W.; Johnson, B. G.; Wong, M. W.; Foresman, J. B.; Robb, M. A.; Head-Gordon, M.; Replogle, E. S.; Gomperts, R.; Andres, J. L.; Raghvachari, K.; Binkley, J. S.; Gonzalez, C.; Martin, R. L.; Fox, D. J.; Defrees, D. J.; Baker, J.; Stewart, J. J. P.; Pople, J. A. GAUSSIAN 94, Gaussian Inc.: Pittsburgh, PA, 1995.

(12) Foresman, J. B.; Frisch, A. In *Exploring Chemistry with Electronic Structure Methods*, 2nd ed.; Gaussian Inc.: Pittsburgh, PA, 1996.

(13) SPARTAN 4.1.1, Wave function Inc.: CA, 1995.

(14) Jurema, M. W.; Shields, G. C. *J. Comput. Chem.* **1993**, *14*, 89.

(15) Gordy, W. *Theoryand Applications of Electron Spin Resonance*; Wiley: New York, 1980.

(16) Stone, E. W.; Maki, A. H. *J. Chem. Phys.* **1962**, *36*, 1944.

(17) Das, M. R; Venkataraman, B. *J. Chem. Phys.* **1961**, *35*, 2262.

(18) Das, M. R.; Fraenkel, G. K. *J. Chem. Phys.* **1965**, *42*, 1350.

(19) Gulick, W. M.; Geske, D. H. *J. Am. Chem. Soc.* **1966**, *88*, 4119.

(20) O'Malley, P. J.; Babcock, G. T. *J. Am. Chem Soc.* **1984**, *106*, 817.

(21) O'Malley, P. J.; Babcock, G. T. *J. Am. Chem Soc.* **1986**, *108*, 3995.

(22) Burghauss, O.; Plato, M.; Rohrer, M.; Mobius, K.; MacMillan, F.; Lubitz, W. *J. Phys. Chem.* **1993**, *97*, 7639.